Solar Energy 202 (2020) 498–506

Contents lists available at ScienceDirect

Solar Energy

journal homepage: www.elsevier.com/locate/solener

Modelling solar cells' S-shaped *I-V* characteristics with an analytical solution to lumped-parameter equivalent circuit model

Fei Yu*, Ying Liang, Xiaofang Sun, Gongyi Huang, Chuanzhong Xu

College of Information Science and Engineering, Huaqiao University, Xiamen 361021, China

A R T I C L E I N F O

Keywords:
Solar cells
S-shaped *I-V* characteristics
Lumped-parameter equivalent circuit model
Analytical solution

A B S T R A C T

In this paper, an analytical solution to three-diode lumped-parameter equivalent circuit model is proposed to simulate and present S-shaped *I-V* characteristics of next generation solar cells, which are observed frequently in perovskite and organic solar cells, and occasionally in other kinds of solar cells. In general, because complicated transcendental equation includes three exponent items resulting from three diodes, the absence of an analytical solution has become a bottleneck that limits the adoptions of solar cells' three-diode lumped-parameter model into practical applications and device simulations. To break through the above bottleneck, the analytical solution is derived in the regional approach, completed in Matlab platform, and verified by reconstructed experimental data measured from real solar cells. Such an analytical solution processes the key feature with high precise and efficiency. High precise results from the mathematical operations of the analytical solution to lumped-parameter model and high efficiency results from the avoidance of numerical iteration methods. In addition, this analytical solution facilitates researchers to accurately determine short circuit current and open circuit voltage, quickly extract model parameters in lumped-parameter circuit, and in detail assess effects from model parameters on DC characteristics of solar cells. Finally, the proposed analytical solution is able to be used to reproduce S-shaped *I-V* characteristics of solar cells, assist in extracting fitting parameters in three-diode lumped-parameter equivalent circuit model, and complete implementation of model into semiconductor device and circuit simulators.

1. Introduction

Utilization of solar energy is very important to the future energy supply and mankind long-term interests. In recent years, solar cells (Yoshikawa et al., 2017) have made rapid progresses towards large-scale commercialization, but the problems of high cost and low power conversion efficiency (PCE) are still plaguing the developments of next generation solar cells. Recently, organic (Wadsworth et al., 2019; Zhou et al., 2018; Park et al., 2018; Meng et al., 2018) and perovskite (Sahli et al., 2018; Jodlowski et al., 2017; Arora et al., 2017; Jiang et al., 2017) solar cells have attracted intensive attentions from researchers because their PCE has increased up to 15–20%. In addition, perovskite and organic solar cells have the advantages of light-weight, low-cost, and soft. This point is also consistent with a disruptive evolution (Petti et al., 2016) of electronics today, advancing from rigid to flexible devices. In fact, researches for perovskite and organic solar cells need to be verified on the basis of analysis for *I-V* characteristics. Therefore, an analytical solution to lumped-parameter model with an ability of accurately and efficiently representing *I-V* curves of perovskite and organic solar cells is urgently necessary for device performance's simulation, analysis, and optimization.

Up to date, lumped-parameter equivalent circuit models could be classified into two categories (Garcia-Sanchez et al., 2017), i.e., conventional one-diode (Banwell and Jayakumar, 2000; Jain and Kapoor, 2004, 2005, Ortiz-Conde et al., 2000, 2012) failing to demonstrate S-shaped DC behaviors (Dunlap-Shohl et al., 2016; Gupta et al., 2019; Kumar and Gaur, 2013; Xu et al., 2016) and non-conventional multiple-diode (Araujo de Castro et al., 2010.; Roland et al., 2016; Yu et al., 2019; Yu et al., 2019; Mazhari, 2006; García-Sánchez et al., 2013) models. At least two diodes in non-conventional multiple-diode models (Araujo de Castro et al., 2010; Roland et al., 2016; Yu et al., 2019; Yu et al., 2019; Mazhari, 2006; García-Sánchez et al., 2013) are used to describe linear (Araujo de Castro et al., 2010), exponential (Roland et al., 2016; Yu et al., 2019), and exponential-like (Yu et al., 2019; Mazhari, 2006; García-Sánchez et al., 2013) S-shaped kinks in *I-V* curves, respectively. Firstly, F. Araujo de Castro's model (Araujo de Castro et al., 2010), including two diodes in lumped-parameter circuit, is proposed and solved by Romero et al. (2012) to reproduce linear S-shaped kinks. Secondly, three-diode lumped-parameter models (Roland et al., 2016; Yu et al., 2019; Yu et al., 2019) are proposed to represent

* Corresponding author.
E-mail address: yufei_jnu@126.com (F. Yu).

https://doi.org/10.1016/j.solener.2020.03.090
Received 11 November 2019; Received in revised form 17 March 2020; Accepted 23 March 2020
Available online 11 April 2020
0038-092X/

exponential-like S-shaped kinks. Mazhari (2006) and García-Sánchez et al. (2013) aimed to describe exponential S-shaped kink. Recently, B. Mazhari's model (Mazhari, May. 2006.) has been solved analytically by Romero et al. (2017) in the special cases and Yu et al. (2019a, 2019bb) in the common cases. Unfortunately, F. J. García-Sánchez's model (García-Sánchez et al., 2013) is still not solved analytically in general. Because numerical iteration solution consumes much computer time and leads to the difficulty in implementing F. J. García-Sánchez's model (García-Sánchez et al., 2013) into device and circuit simulator, the absence of the common analytical solution actually limits the practical applications of F. J. García-Sánchez's model (García-Sánchez et al., 2013).

In this paper, the analytical solution to terminal current-voltage equation of F. J. García-Sánchez's lumped-parameter equivalent circuit model is derived in the regional approach to accurately and efficiently describe *I-V* characteristics of perovskite and organic solar cells. In fact, simulation and analysis for *I-V* characteristics, especially for S-shaped kink, are both foundation and key to researches and optimizations on materials, structures, and processes of solar cells. And then, short circuit current I_{sc} and open circuit voltage V_{oc} are determined. Furthermore, analysis for effects from model parameters on *I-V* characteristics is also provided to give references for optimization of solar cells. Finally, numerical iteration results and reconstructed experimental data measured from real solar cells are used to verify the accuracy and practicability of the proposed analytical solution. As a result, such a solution actually is able to perform accurate and efficient simulations for S-shaped *I-V* characteristics of perovskite and organic solar cells and become a useful tool for implementing F. J. García-Sánchez's model into photovoltaic device and circuit simulators.

2. Analytical solution to S-shaped *I-V* characteristics of solar cells

In 2013, García-Sánchez et al. (2013) made a minor but crucial modification for F. Araujo de Castro's model (Araujo de Castro et al., 2010) by substituting a diode for resistor in lumped-parameter equivalent circuit, as shown in Fig. 1. Obviously, F. J. García-Sánchez's model (García-Sánchez et al., 2013) instead of B. Mazhari's model (Araujo de Castro et al., 2010) consists of two sub-circuits, which play clearer roles in producing S-shaped *I-V* curves, conforming to the multilayer structures of the current solar cells. Here, sub-circuit 1 is the conventional one-diode lumped-parameter model, representing J-shape *I-V* curves of solar cells. In sub-circuit 1, I_{ph} is a light generated current source depending on irradiation intensity, the current through the first diode D_1 is the diffusion and recombination current in the quasi neutral regions of solar cells, the current through a shunt resistor R_{sh} is the leakage current depending on PN junction, and R_s is the series resistor depending on contact resistors. In Fig. 1, Sub-circuit 2 is in series with the sub-circuit 1. In Sub-circuit 2, D_2 is the second diode with opposite polarity describing the detrimental S-shaped concave region of the illuminated solar cell *I-V* curves in 0 V $< V < V_{oc}$, and D_3 is the third diode with positive polarity replacing for the resistor in F. Araujo de Castro's model (Araujo de Castro et al., 2010) to demonstrate exponential S-shaped kinks of *I-V* curves in $V > V_{oc}$.

According to Fig. 1, the terminal voltage V is given by the sum of V_s, V_1, and V_2, i.e.,

$$V = V_s + V_1 + V_2. \tag{1}$$

Based on Ohm's law and Shockley's ideal diode current equation (Shockley, 1949); V_s, V_1, and V_2 are implied in the following equations:

$$I = \frac{V_s}{R_s}, \tag{2}$$

$$I = \frac{V_1}{R_{sh}} + I_{01}\left(e^{\frac{V_1}{n_1 V_t}} - 1\right) - I_{ph}, \tag{3}$$

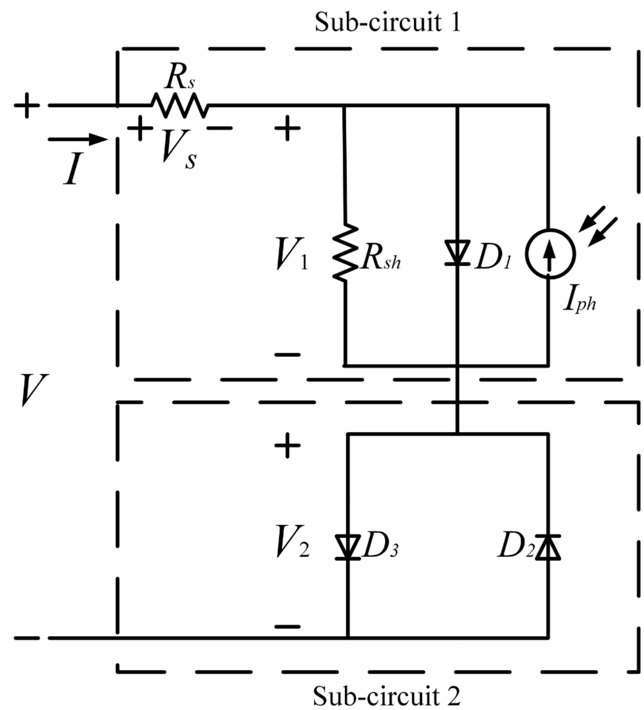

Fig. 1. Previous proposed lumped-parameter equivalent circuit model (García-Sánchez et al., 2013), consisting of a conventional one-diode solar cell lumped-parameter equivalent sub-circuit 1 and an exponential S-shape curve producing sub-circuit 2.

$$I = -I_{02}\left(e^{\frac{-V_2}{n_2 V_t}} - 1\right) + I_{03}\left(e^{\frac{V_2}{n_3 V_t}} - 1\right). \tag{4}$$

Here, for D_1, D_2, and D_3, I_{01}, I_{02}, I_{03} are the reverse saturation currents, n_1, n_2, and n_3 are the ideality factors representing the divergence from the ideal diode.

In order to obtain the analytical solution to terminal *I-V* characteristics in Fig. 1, V_s, V_1, and V_2 as a function of I should be solved analytically from (2) to (4), respectively. On the one side, V_s and V_1 can be solved directly from (2) and (3). (2) is only a linear equation, yielding

$$V_s = IR_s. \tag{5}$$

(3) is a transcend equation including only one exponent item, so that V_1 is derived by using lambert W function's principal branch (Corless et al., 1996):

$$V_1 = (I_{ph} + I_{01} + I)R_{sh} - n_1 V_t \times W_0\left[\frac{I_{01}R_{sh}}{n_1 V_t}\cdot e^{\frac{(I_{ph}+I_{01}+I)R_{sh}}{n_1 V_t}}\right], \tag{6}$$

where W_0 is a typical solution to equation $W_0(x) \bullet e^{W_0(x)} = x$. On the other side, (4) is also a transcend equation, but includes two exponent items. This is the reason why V_2 cannot be derived directly from (4). By making $x = e^{V_2/n_2 V_t}$ and analyzing (4) carefully, (4) is transformed mathematically as

$$I_{03}\cdot x^{1+\frac{n_2}{n_3}} - (I - I_{02} + I_{03})\cdot x - I_{02} = 0. \tag{7}$$

From (7), V_2 or x can only be solved on the condition that n_2/n_3 is the integer < 4, because at most quartic equation with one unknown variable could be solved analytically. For the other ratios of n_2/n_3, V_2 has to be solved from (7) in numerical iteration methods, such as Newton-Raphson method (Yu et al., 2019). Obviously, numerical iteration methods would consume a lot of computer resources and much amount of computation time, which would result in the difficulty of implementing lumped-parameter model of Fig. 1 into simulators and limit the range of model's practical applications. Therefore, the improvement rooms are left for us to search for an accurate and efficient method of deriving V_2 from (4) analytically as follows.

In fact, the root reason why an analytical solution V_2 cannot be derived generally from (4) is that two exponents e^{-V_2/n_2V_t} and e^{V_2/n_3V_t} exist in the transcend Eq. (4). Fortunately, based on the regional approach, an analytical solution to V_2 can be derived. In the regional approach, the different mathematical expressions individually describe the different regimes of solar cells' operation, and then these mathematical expressions are combined by smoothing function into a single equation. Of course, this regional approach has been applied in many kinds of semiconductor device models (Yu et al., 2016; Fang et al., 2017; Yu et al., 2017; Ghittorelli et al., 2015).

In the operation regime of $V_2 < 0$ V, the exponent item e^{-V_2/n_2V_t} dominates the right hand side (RSH) of (4), because e^{V_2/n_3V_t} trends to be zero. Then, (4) can be simplified as

$$I = -I_{02}\left(e^{\frac{-V_{2-sub1}}{n_2V_t}} - 1\right) - I_{03}, \tag{8}$$

where $V_{2\text{-}sub1}$ is an approximate solution to V_2, which is only valid in the operation region of $V_2 < 0$ V:

$$V_{2-sub1} = -n_2V_t\cdot\ln\left(\frac{I - I_{02} + I_{03}}{I_{02}}\right). \tag{9}$$

In the operation regime of $V_2 > 0$ V, e^{V_2/n_3V_t} is the dominant exponent item in the RSH of (4), because e^{-V_2/n_2V_t} trends to be zero. Then, (4) can be simplified as

$$I = I_{02} + I_{03}\left(e^{\frac{V_{2-sub2}}{n_3V_t}} - 1\right), \tag{10}$$

where $V_{2\text{-}sub2}$ is an aymptotic solution to V_2, which is only valid in the operation region of $V_2 > 0$ V:

$$V_{2-sub2} = n_3V_t\cdot\ln\left(\frac{I - I_{02} + I_{03}}{I_{03}}\right). \tag{11}$$

Based on the idea of the regional approach, a smoothing function in mathematics must be adopted to connect $V_{2\text{-}sub1}$ in (9) and $V_{2\text{-}sub2}$ in (11), aiming to acquire the expression of V_2 which is valid for the whole operational region. In order to complete the connection successfully, the following mathematical operations are performed. Firstly, the minimum value $V_{2\text{-}sub1\text{-}min}$ and position pointer i_{min} are searched from (9): $[V_{2sub1\text{-}min}, i_{min}]$ = Min ($V_{2\text{-}sub1}$); the maximum value $V_{2\text{-}sub2\text{-}max}$ and position pointer i_{max} are searched from (11): $[V_{2\text{-}sub2\text{-}max}, i_{max}]$ = Max ($V_{2\text{-}sub2}$); it is noted that $i = i_{min} = i_{max}$. Secondly, the intersection point (V_x, I_x) is determined by using $e^{-V_x/n_2V_t} = e^{V_x/n_3V_t}$ as

$$V_x = \frac{n_2n_3V_t}{n_2 + n_3}\cdot\ln\left(\frac{I_{02}}{I_{03}}\right), \tag{12}$$

$$I_x = -I_{02}\left(e^{\frac{-V_x}{n_2V_t}} - 1\right) + I_{03}\left(e^{\frac{V_x}{n_3V_t}} - 1\right). \tag{13}$$

Thirdly, amplification factor F_a is determined as

$$F_a = \frac{Max(V_{2-sub2-max} - V_x,\ V_x - V_{2-sub1-min})}{Min(V_{2-sub2-max} - V_x,\ V_x - V_{2-sub1-min})}. \tag{14}$$

Fourthly, the inaccurate areas of $V_{2\text{-}sub1}$ and $V_{2\text{-}sub2}$ are transformed and amplified, respectively, yielding

$$\begin{aligned} &V_{2-sub1}(V < V_{2-sub1-max}) = -n_2V_t\cdot\ln\left(\tfrac{I - I_{02} + I_{03}}{I_{02}}\right),\\ &V_{2-sub1}(V > V_{2-sub1-max}) = F_a \times \left[2V_{2-sub1-max} + n_2V_t\cdot\ln\left(\tfrac{I - I_{02} + I_{03}}{I_{02}}\right)\right]; \end{aligned} \tag{15}$$

and

$$\begin{aligned} &V_{2-sub2}(V < V_{2-sub2-min}) = F_a \times \left[2V_{2-sub2-min} - n_3V_t\cdot\ln\left(\tfrac{I - I_{02} + I_{03}}{I_{03}}\right)\right],\\ &V_{2-sub2}(V > V_{2-sub2-min}) = n_3V_t\cdot\ln\left(\tfrac{I - I_{02} + I_{03}}{I_{03}}\right). \end{aligned} \tag{16}$$

Finally, the following smoothing function (Yu et al., Mar. 2016) is used to connect $V_{2\text{-}sub1}$ in (15) and $V_{2\text{-}sub2}$ in (16) into a unified solution of V_2 valid in the whole operation region as

$$V_2 = \frac{1}{m}\ln\left(\frac{1}{1/e^{mV_{2-sub1}} + 1/e^{mV_{2-sub2}}}\right). \tag{17}$$

Here, m is a weight parameter more than 10 generally, determining the sharpness of the change from $V_{2\text{-}sub1}$ to $V_{2\text{-}sub2}$.

In order to improve the accuracy of V_2 in (17), Schroder series w is used to refresh V_2 as

$$V_2 = V_2 + w, \tag{18}$$

$$w = \frac{y/y'}{1 - 0.5yy''/y'^2}, \tag{19}$$

$$y = -I_{02}\left(e^{\frac{-V_2}{n_2V_t}} - 1\right) + I_{03}\left(e^{\frac{V_2}{n_3V_t}} - 1\right) - I. \tag{20}$$

$$y' = \frac{I_{02}e^{\frac{-V_2}{n_2V_t}}}{n_2V_t} + \frac{I_{03}e^{\frac{V_2}{n_3V_t}}}{n_3V_t}, \tag{21}$$

$$y'' = -\frac{I_{02}e^{\frac{-V_2}{n_2V_t}}}{(n_2V_t)^2} + \frac{I_{03}e^{\frac{V_2}{n_3V_t}}}{(n_3V_t)^2}. \tag{22}$$

Here, Schroder series w is able to make the absolute error of V_2 as low as 1fV scale. Compared with (17), (18) is much more accurate. Therefore, (18) is the analytical solution to V_2 in (4). Now, by substituting V_s in (5), V_1 in (6), and V_2 in (18) into (1), the analytical solution to terminal voltage V of Fig. 1 is acquired.

In the three cases of $n_2/n_3 = 1$, 2, and 3, the analytical solutions to V_2 derived by García-Sánchez et al. (2013) are used to initially evaluate the above proposed analytical algorithm for solving V_2 in (4). The analytical solution to V_2 solved by F. J. García-Sánchez and us in the cases of $n_2/n_3 = 1$, 2, and 3 are shown in Figs. 2–4, respectively. Good agreements demonstrate the accuracy of our analytical solution for the above special three cases. As shown in Figs. 2–4, $V_{2\text{-}sub1}$ is accurate in the region of $V_2 < V_x$, but incorrect in the region of $V_2 > V_x$. On the contrary, $V_{2\text{-}sub2}$ is false in the region of $V_2 < V_x$, but right in the region of $V_2 > V_x$.

3. Determinations of short circuit current and open circuit voltage

In the real solar cells, the short circuit current I_{sc} and open circuit voltage V_{oc} are two important parameters in the *I-V* characteristics. In the case of short circuit for Fig. 1, $V = 0$ V and $I = I_{sc}$. The following equations are acquired as

$$I_{sc} = I_{03}\left(e^{\frac{V_{2-sc}}{n_3V_t}} - 1\right) - I_{02}\left(e^{\frac{-V_{2-sc}}{n_2V_t}} - 1\right), \tag{23}$$

$$I_{sc} = I_{01}\left(e^{\frac{-V_{2-sc}-I_{sc}R_s}{n_1V_t}} - 1\right) - \frac{V_{2-sc} + I_{sc}R_s}{R_{sh}} - I_{ph}. \tag{24}$$

In (23) and (24), there are two unknown variables, i.e., short circuit current I_{sc} and voltage $V_{2\text{-}sc}$ across the third diode. Here, by substituting (23) into (24) and eliminating I_{sc}, the implicit equation of $V_{2\text{-}sc}$ could be solved easily in Newton-Raphson method. Then, substituting the value of $V_{2\text{-}sc}$ into (23), the calculation result of I_{sc} can be obtained. In the case of open circuit for Fig. 1, $I = 0$A and $V = V_{oc}$. The equation of V_{oc} is given as

$$\frac{V_{oc}}{R_{sh}} + I_{01}\left(e^{\frac{V_{oc}}{n_1V_t}} - 1\right) - I_{ph} = 0. \tag{25}$$

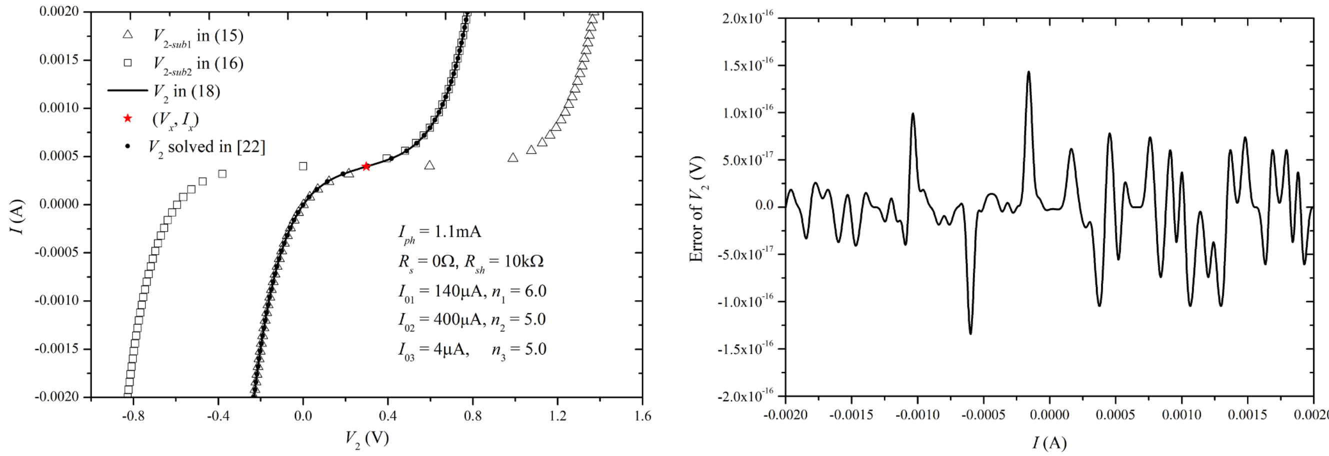

Fig. 2. (a) I vs. V_2 curves in the case of $n_2/n_3 = 1$, (b) error of V_2 between the proposed analytical solution and F. J. García-Sánchez's solution (García-Sánchez et al., 2013).

Obviously, only one exponent is included in the transcend equation (25). Then, based on the Lambert W function (Corless et al., 1996); V_{oc} is solved analytically as

$$V_{oc} = (I_{01} + I_{ph})R_{sh} - n_1 V_t \cdot W_0\left(\frac{I_{01}R_{sh}}{n_1 V_t}\cdot e^{\frac{I_{01}R_{sh}+I_{ph}R_{sh}}{n_1 V_t}}\right). \tag{26}$$

4. Verifications and discussions

In this part, numerical iteration simulation results and reconstructed experimental data are used to verify our proposed analytical solution to lumped-parameter equivalent circuit model of solar cells in Fig. 1. On the one hand, numerical iteration methods can be used to solve the general solution to three-diode model in Fig. 1. Numerical iteration methods are convenient for researchers to study and discuss the effects from model parameters on I-V characteristics of solar cells, but they would take up a lot of computer resources and spend much computation time on the loops of numerical iteration methods. In fact, iteration's low computational efficiency limits the implement of lumped-parameter equivalent circuit model into solar cells' simulators. However, high precision of numerical iteration solution can be used to verify the accuracy of our proposed analytical solution to lumped-parameter equivalent circuit model of solar cells in Fig. 1. On the other hand, reconstructed experimental data measured from real perovskite and organic solar cells are used to validate the practicability of our proposed analytical solution to F. J. García-Sánchez's model (García-Sánchez et al., 2013).

Numerical iteration methods, such as Newton-Raphson method (Huang et al., 2018; Xu et al., 2018; Yu et al., 2019), can also be used to solve V_1 in (3) and V_2 in (4). Then, V_s, V_1, and V_2 are substituted into (1) to obtain the results of V in Fig. 1 and describe the I-V curves of perovskite and organic solar cells. In fact, numerical iteration methods can be used to solve and integrate lumped-parameter equivalent circuit model into photovoltaic device simulator, such as Silvaco Atlas Device Simulation Framework (https://www.silvaco.com/products/tcad/device_simulation/atlas/atlas.html), owing to high computational accuracy. However, numerical iteration methods fail to perform its duty in circuit and system simulators, due to low computational efficiency. Obviously, because of high precise of numerical iteration methods, numerical iteration solution to lumped-parameter equivalent circuit model can be used to verify the accuracy of our proposed analytical solution, especially for the cases of arbitrary n_2 / n_3. In Fig. 5, good agreements between our proposed analytical solution and Newton-Raphson method solution can be observed in Fig. 5(a) and error of V locates within the scope of 6×10^{-16} V, as shown in Fig. 5(b). Of course, compared with Newton-Raphson method, our proposed analytical solution consumes much less computation time. Firstly, according to Fig. 5(a), I-V_1 curve (green line) represents the conventional J-shaped I-V characteristics observed in classical silicon-based solar cells and I-V_2 curve (blue line) actually demonstrates the exponential kink in the region of $V > 0$ V. Secondly, short-circuit point (0, I_{sc}), open-circuit point (V_{oc}, 0), the corresponding point (V_m, I_m) of maximum power

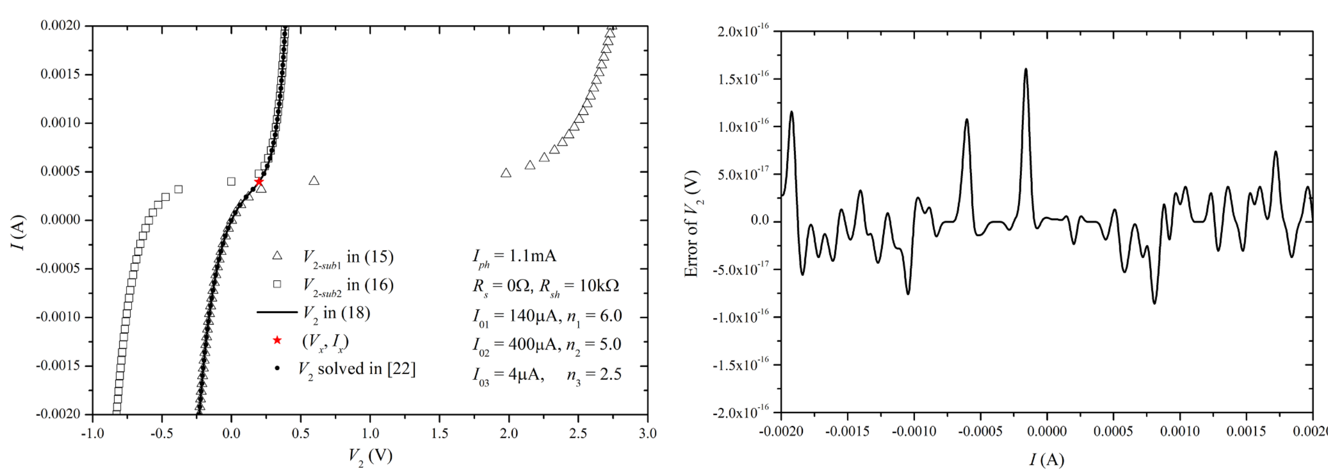

Fig. 3. (a) I vs. V_2 curves in the case of $n_2/n_3 = 2$, (b) error of V_2 between the proposed analytical solution and F. J. García-Sánchez's solution (García-Sánchez et al., 2013).

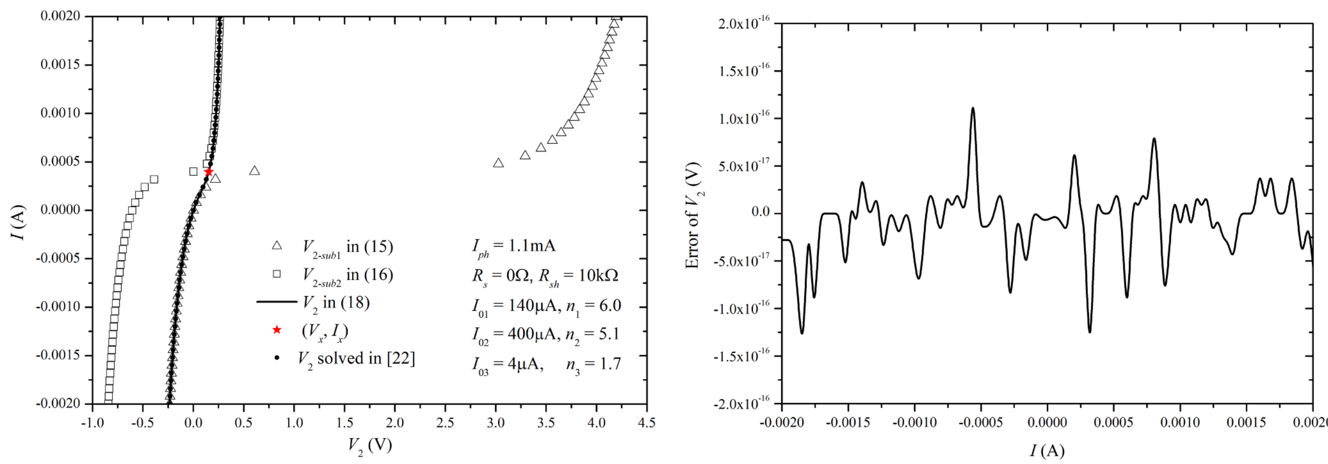

Fig. 4. (a) I vs. V_2 curves in the case of $n_2/n_3 = 3$, (b) error of V_2 between the proposed analytical solution and F. J. García-Sánchez's solution (García-Sánchez et al., 2013).

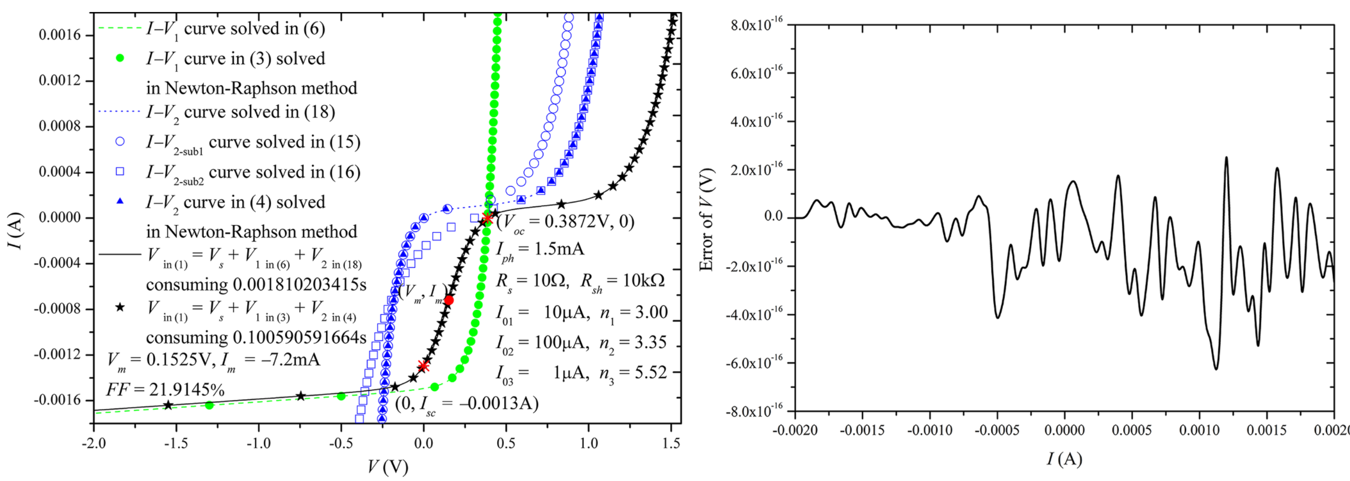

Fig. 5. (a) I vs. V_1, V_2, and V curves in the case of arbitrary $n_2 / n_3 = 3.35/5.52$, (b) error of V between the proposed analytical solution and Newton-Raphson method solution.

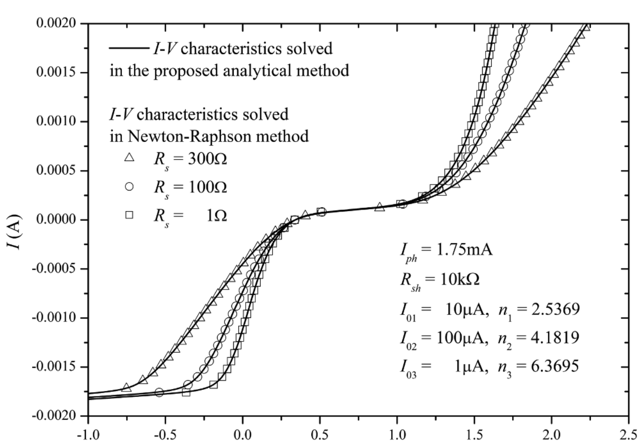

Fig. 6. I vs. V curves simulated by lumped-parameter model in Fig. 1 with the different R_s.

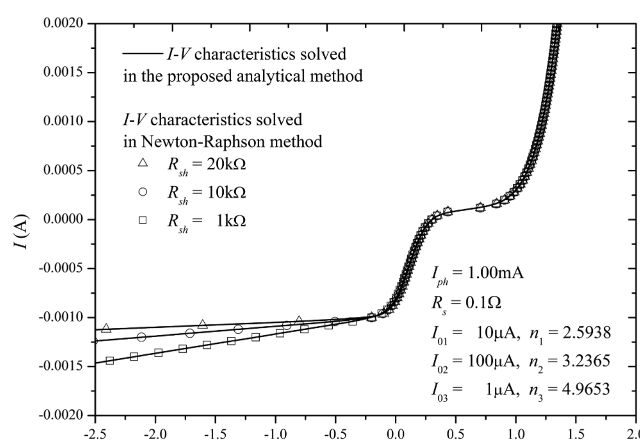

Fig. 7. I vs. V curves simulated by lumped-parameter model in Fig. 1 with the different R_{sh}.

point, and fill factor *FF* are calculated and shown in Fig. 5(a). Thirdly, *I-V* curve (black line) describes the S-shaped *I-V* characteristics of perovskite and organic solar cells with the exponential kink. In the region of $V < 0$ V or $I < I_{sc}$, *I-V* curve (black line) is dominated by *I-V_1* curve (green line). In the most important region of $0\text{ V} < V < V_{oc}$ or $I_{sc} < I < 0$A, *I-V* curve (black line) contains the information of power conversion efficiency (PCE) and fill factor (*FF*), which is reduced from *I-V_1* curve (green line) to *I-V* curve (black line) under the influence of *I-$V_{2\text{-sub1}}$* curve (blue circle symbols). In other words, *I-$V_{2\text{-sub1}}$* curve (blue circle symbols) or *I-V_2* curve (blue line) in the scope of $0\text{ V} < V < V_{oc}$

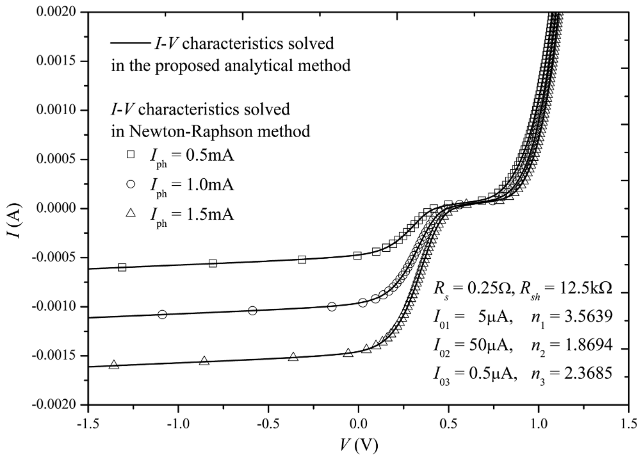

Fig. 8. *I* vs. *V* curves simulated by lumped-parameter model in Fig. 1 with the different I_{ph}.

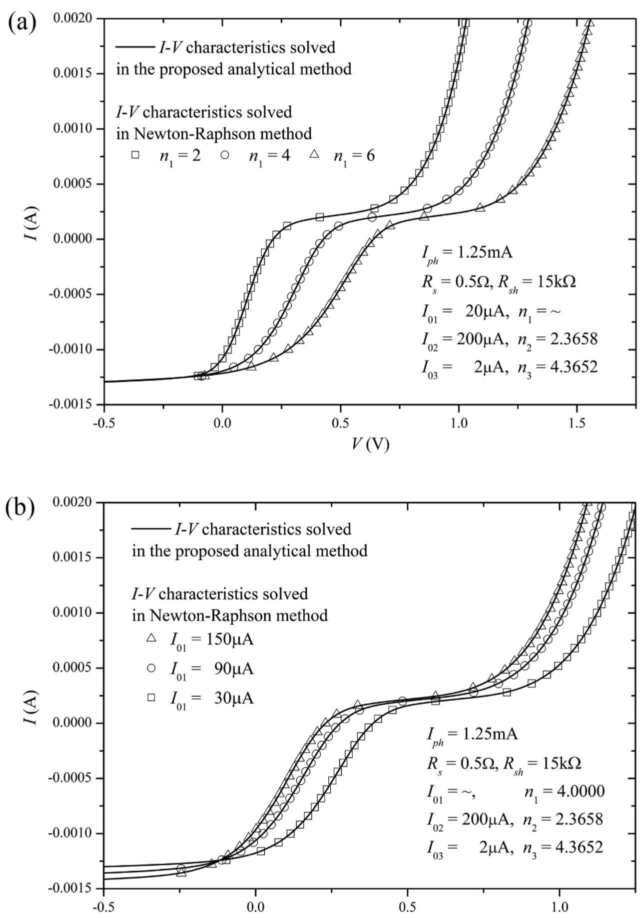

Fig. 9. *I* vs. *V* curves simulated by lumped-parameter model in Fig. 1 with the different n_1 and I_{01}: (a) for n_1, (b) for I_{01}.

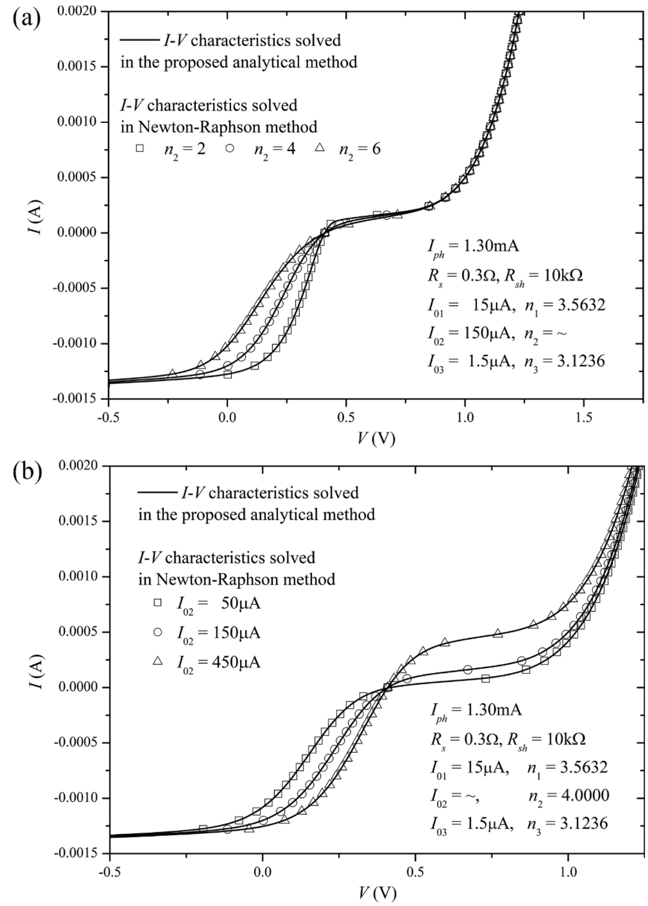

Fig. 10. *I* vs. *V* curves simulated by lumped-parameter model in Fig. 1 with the different n_2 and I_{02}: (a) for n_2, (b) for I_{02}.

determines the deviations of PCE and *FF* from *I-V*$_1$ curve (green line) to *I-V* curve (black line). In the region of $V > V_{oc}$ or $I > 0$A, *I-V* curve (black line) shows the exponential kink of *I* which is affected by *I-V*$_{2\text{-sub2}}$ curve (blue square symbols).

Furthermore, we discuss the effects from circuit components on *I-V* characteristics of perovskite and organic solar cells in Figs. 6–11. Firstly, considering that R_s locates on the main path of *I*, it is capable to influence the whole regions of *I-V* curves, as shown in Fig. 6. Especially, R_s has an important role in reducing PCE, *FF*, and exponential kink. Secondly, as the conventional single-one diode lumped-parameter equivalent circuit model, R_{sh}, I_{ph}, and D_1 in the sub-circuit 1 of Fig. 1 can change graphical shapes of *I-V* curves in $V < V_{oc}$ or generate graphical translations of *I-V* curves in $V > V_{oc}$. It is noted that these devices are not able to affect graphical shapes of *I-V* curves in $V > V_{oc}$, because exponential kink is depending on V_2 in (4) instead of V_1 in (3). In Fig. 7, R_{sh} only affects the region of $V < 0$ V rather than that of $V > 0$ V, i.e., it has no impact on PCE, *FF*, and exponential kink. This point is consistent with the analysis on *I-V* characteristics represented by (3) and (4). In Fig. 8, I_{ph} would significantly affect I_{sc} according to (24), but slightly affect V_{oc} according to (26). In Fig. 9, the current through D_1 has a positive correlation with the increase of *I-V* curves in the region of $0\text{ V} < V < V_{oc}$. Then, lower current through D_1 is corresponding to larger *FF*. Thirdly, D_2 and D_3 in the sub-circuit 2 of Fig. 1 can nearly determine *I-V*$_{2\text{-sub1}}$ and *I-V*$_{2\text{-sub2}}$ curves, respectively. As shown in Figs. 10 and 11, n_2 and I_{02} affect the region of $0\text{ V} < V < V_{oc}$ where $V_{2\text{-sub1}}$ is the dominant item for V_2, while n_3 and I_{03} affect the region of $V > V_{oc}$ where $V_{2\text{-sub2}}$ is the dominant item for V_2.

In fact, S-shaped *I-V* characteristics are usually observed in a new generation solar cells represented by perovskite and organic solar cells. And then, exponential kinks in S-shaped *I-V* curves generally appear in the cases of low operational temperature (Xu et al., 2016), thin cathode layer (Sesa et al., 2019), low annealing temperature (De Castro et al., 2016), etc. In order to validate the practicability of our analytical solution to lumped-parameter equivalent circuit model in Fig. 1, based on the above analysis for effects from single model parameter on *I-V* characteristics, we compare our analytical solutions with the reconstructed experimental data from real perovskite (Xu et al., 2016) and organic (Sesa et al., 2019) solar cells in Figs. 12–14. The parameters used in simulations are listed in Tables 1 and 2, that can be extracted

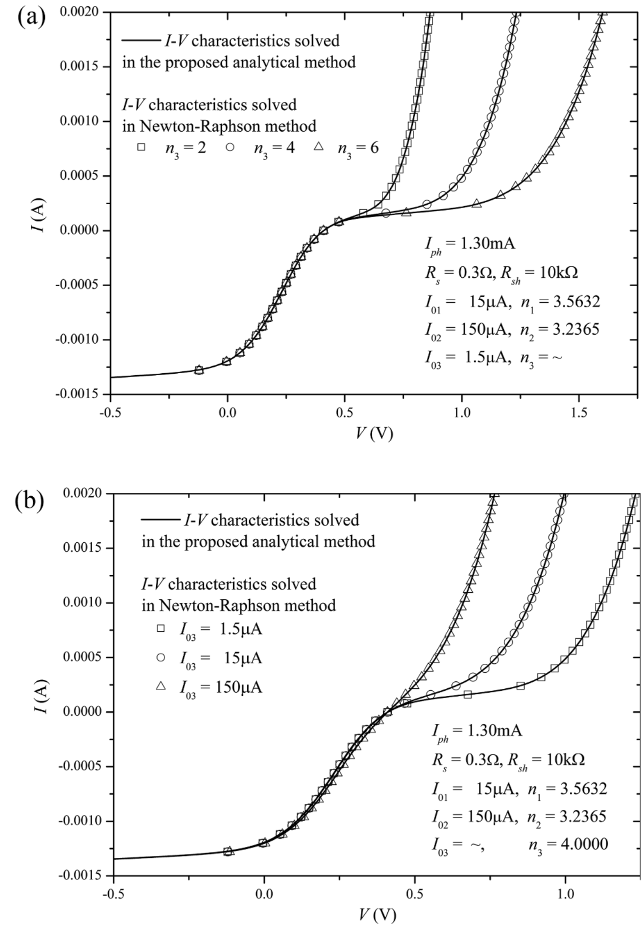

Fig. 11. I vs. V curves simulated by lumped-parameter model in Fig. 1 with the different n_3 and I_{03}: (a) for n_3, (b) for I_{03}.

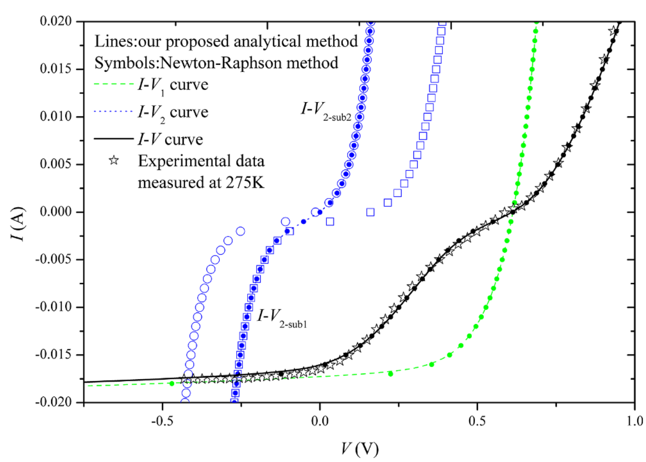

Fig. 12. Comparisons between simulation results of our analytical solution to lumped-parameter model in Fig. 1 and reconstructed experimental data (Xu et al., 2016) measured from planar perovskite solar cells at 275 K. Parameters used in simulations are listed in Table 1.

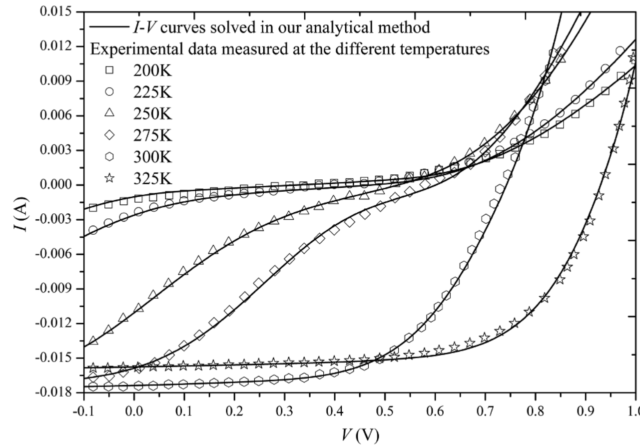

Fig. 13. Comparisons between simulation results of our analytical solution to lumped-parameter model in Fig. 1 and reconstructed experimental data (Xu et al., 2016) measured from planar perovskite solar cells at the different operating temperatures varied from 200 K to 325 K. Parameters used in simulations are listed in Table 1.

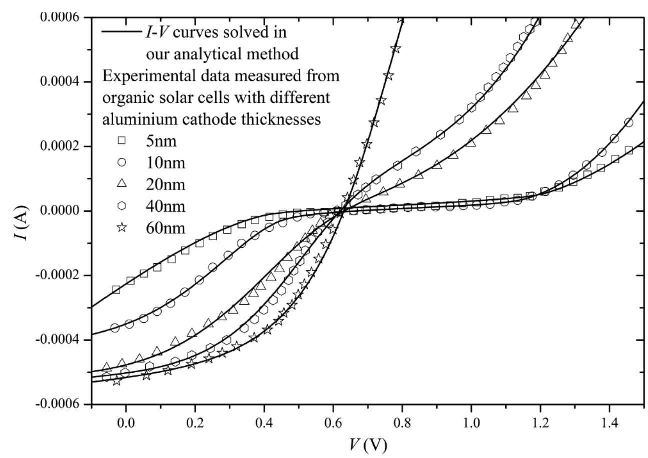

Fig. 14. Comparisons between simulation results of our analytical solution to lumped-parameter model in Fig. 1 and reconstructed experimental data (Sesa et al., 2019) measured from organic solar cells with the different thicknesses of aluminum cathode varied from 5 nm to 60 nm. Parameters used in simulations are listed in Table 2.

Table 1
Parameters used in simulations for I-V Curves in Figs. 12 and 13.

Symbol (unit)	200 K	225 K	250 K	275 K	300 K	325 K
I_{ph} (mA)	17.5	17.5	17.5	17.5	17.5	15.8
R_s (Ω)	17.2	12.0	5.5	1.0	0.5	0.1
R_{sh} (kΩ)	1.0	1.0	1.5	1.5	1.5	1.5
n_1 (–)	3.0	4.0	3.85	3.8	3.8	3.8
I_{01} (μA)	60	30	30	30	4.5	0.5
n_2 (–)	6.0	6.0	6.0	4.9	3.2	3.0
I_{02} (μA)	50	50	550	1.0×10^3	10×10^3	20×10^3
n_3 (–)	5.0	4.3	4.0	3.8	1.5	1.2
I_{03} (μA)	45	300	800	1.1×10^3	4.0×10^3	6.0×10^3

through the common routine of the parameter acquisition (Wei et al., 2019) based on intelligent computational algorithms.

Planar perovskite solar cells (Xu et al., 2016) were fabricated by one-step solution process. The perovskite solar cell (Xu et al., 2016) consists of 200 nm fluorine-doped thin oxide (FTO) glass substrates, 30 nm compact TiO2 layer, 300 nm perovskite absorber layer, 500 nm hole-transporting material (HTM) layer, and Au electrode deposited by thermal evaporation, respectively. The photovoltaic properties of the planar perovskite solar cells were characterized by I–V measurements under AM1.5G (100 mW/cm^2) illumination at the different operating temperatures varied from 200 K to 325 K. In Fig. 12, at the operating temperature 275 K, both our analytical solution and numerical iteration solution to lumped-parameter equivalent circuit model in Fig. 1 are able to accurately simulate I–V properties of perovskite solar cells. It is noted that, I–V_1 curve directly determines I–V curve in the region of

Table 2
Parameters used in simulations for *I-V* Curves in Fig. 14.

Symbol (unit)	5 nm	10 nm	20 nm	40 nm	60 nm
I_{ph} (mA)	0.52	0.52	0.52	0.52	0.52
R_s (Ω)	1000	500	200	5	0.5
R_{sh} (kΩ)	100	100	40	35	10
n_1 (–)	10.0	6.8	6.3	6.2	3.8
I_{01} (μA)	100	100	7.5	7.5	7.5
n_2 (–)	1.0	2.0	2.5	3.5	1.3
I_{02} (μA)	1.5	1.6	30	120	600
n_3 (–)	3.0	3.3	8.8	8.8	1.8
I_{03} (μA)	0.015	0.08	70	60	60

$V < 0$ V, both I–V_1 and I–$V_{2\text{-sub1}}$ determine I–V curve in the region of $0 \text{ V} < V < V_{oc}$, and both I–V_1 and I–$V_{2\text{-sub2}}$ determine I–V curve in the region of $V > V_{oc}$. As shown in Fig. 13, at the different operating temperatures varied from 200 K to 325 K, our analytical solution results can still show good agreements with experimental data. Below the room temperature 300 K, *I–V* characteristics of perovskite solar cells obviously show S-shaped curves with exponential kink. However, above the room temperature 300 K, *I–V* curves of perovskite solar cells remain to be J-shaped. Considering that measurements are completed under the same solar irradiation AM1.5G (100 mW/cm^2) in Fig. 13, the values of photovoltaic current I_{ph} at the different operating temperatures from 200 K to 300 K remain unchanged in Table 1. In addition, because I_{ph} depends on cell's operating temperature (Enrique et al., 2007) (Villalva et al., 2009); I_{ph} is settled as a relatively low value above the room temperature. As the operating temperature increases, R_s decreases from 17.2 Ω at 200 K to 0.1 Ω at 325 K. In addition, with an increment of the operating temperature, R_{sh} and the currents through $D_2 \sim D_3$ increase while the current through D_1 decreases. Of course, these above points are consistent with semiconductor device physics.

S-shaped profile is also a common feature of *I-V* curves of organic solar cells (Sesa et al., 2019; De Castro et al., 2016). A case verification based on ITO/PEDOT-PSS/P3HT:PCBM/Al solar cells (Sesa et al., 2019) whose *I-V* curves transform from S-shape to J-shape with increasing aluminum thickness, as shown in Fig. 14. In the processes, patterned indium tin oxide (ITO) substrates were sourced from Kintec firstly, 70 μl of poly (3,4-ethylenedioxythiophene)/(poly(styrenesulfonate) (PEDOT:PSS, Baytron P) solution was spin-coated onto each ITO slide secondly, the PEDOT:PSS coated substrates were then placed on a hotplate and dried, the P3HT:PCBM solution was deposited by pipetting 65 μl of solution onto each PEDOT:PSS covered substrate and then spreading it evenly across the surface using the pipette tip, the series of aluminum-only electrodes deposited were designed to have individual layer thickness of 5 nm, 10 nm, 20 nm, 40 nm, 60 nm, finally. In Fig. 14, we can observe that aluminum cathode thickness is less than 60 nm, *I-V* curves of organic solar cells show S-shape with exponential kink. On the condition that aluminum cathode thickness is larger than 60 nm, J-shaped *I-V* curve is observed in organic solar cells. For these two cases, our analytical solution to the lumped-parameter equivalent circuit model in Fig. 1 is still able to accurately and efficiently simulate the *I-V* characteristics measured from organic solar cells (Sesa et al., 2019).

5. Conclusions

In this paper, based on the regional approach, we non-iteratively derived an analytical solution to three-diode lumped-parameter equivalent circuit model with the ability of simulating the S-shaped *I-V* characteristics with exponential kinks. Furthermore, we determine short-circuit current and open-circuit voltage of solar cells. Finally, we use numerical iteration results and reconstructed experimental data measured from perovskite and organic solar cells to verify the accuracy and applicability of our analytical solution. The verification results demonstrate that our analytical solution is an important tool of explaining S-shaped *I-V* characteristics with exponential kinks in perovskite and organic solar cells and implementing three-diode lumped-parameter equivalent circuit model into photovoltaic device and circuit simulators.

Declaration of Competing Interest

The authors declare that they have no known competing financial interests or personal relationships that could have appeared to influence the work reported in this paper.

Acknowledgment

This work was supported in part by in part by the National Natural Science Foundation of China under grant 61904056, the Scientific Research Funds for the Young Teachers of Fujian Province under grant JAT170034, and in part by the Scientific Research Funds of Huaqiao University under grant 16BS706.

References

Araujo de Castro, F., Heier, J., Nüesch, F., Hany, R., 2010. Origin of the kink in current-density versus voltage curves and efficiency enhancement of polymer-C60 heterojunction solar cells. IEEE J. Sel. Top. Quantum Electron. 16 (6), 1690–1699.
Arora, N., Dar, M.I., Hinderhofer, A., Pellet, N., Schreiber, F., Zakeeruddin, S.M., Gratzel, M., 2017. Perovskite solar cells with CuSCN hole extraction layers yield stabilized efficiencies greater than 20%. Science 358 (6364), 768–771.
Banwell, T., Jayakumar, A., 2000. Exact analytical solution for current flow through diode with series resistance. Electron. Lett. 36 (4), 291–292.
Corless, R.M., Gonnet, G.H., Hare, D.E.G., Jeffrey, D.J., Knuth, D.E., 1996. On lambert's W function. Adv. Comput. Math. 5 (1), 329–359.
De Castro, F., Laudani, A., Fulginei, F.R., Salvini, A., 2016. An in-depth analysis of the modelling of organic solar cells usingmultiple-diode circuits. Sol. Energy 135, 590–597.
Dunlap-Shohl, W.A., Younts, R., Gautam, B., Gundogdu, K., Mitzi, D.B., 2016. Effects of Cd diffusion and doping in high-performance perovskite solar cells using CdS as electron transport layer. J. Phys. Chem. 120 (30), 16437–16445.
Enrique, J.M., Duran, E., Sidrach-de-Cardona, M., Andujar, J.M., 2007. Theoretical assessment of the Maximum power point tracking efficiency of photovoltaic facilities. Sol. Energy 81 (1), 31–38.
Fang, J., Deng, W., Ma, X., Huang, J., Wu, W., 2017. A surface-potential-based DC model of amorphous oxide semiconductor TFTs including degeneration. IEEE Electron Dev. Lett. 38 (2), 183–186.
García-Sánchez, F.J., Lugo-Muñoz, D., Muci, J., Ortiz-Conde, A., 2013. Lumped parameter modeling of organic solar cells' S-shaped I-V Characteristics. IEEE J. Photovoltaics 3 (1), 330–335.
Garcia-Sanchez, F.J., Romero, B., Lugo-Munoz, D.C., Del Pozo, G., Arredondo, B., Liou, J.J., Ortiz-Conde, A., 2017. Modelling solar cell S-Shaped I-V characteristics with DC lumped-parameter equivalent circuits – a review. Facta Univ. – Ser. Electron. Energet. 30 (3), 327–350.
Ghittorelli, M., Torricelli, F., Kovacs-Vajna, Z.M., 2015. Analytical physical-based drain-current model of amorphous InGaZnO TFTs accounting for both non-degenerate and degenerate conduction. IEEE Electron Dev. Lett. 36 (12), 1340–1343.
Gupta, S.K., Banerjee, S., Singh, A., Pali, L.S., Garg, A., 2019. Modeling of degradation in normal and inverted OSC devices. Sol. Energy Mater. Sol. Cells 191 (3), 329–338.
Huang, G., Yu, F., Xu, C., 2018.. An analytical solution to lumped parameter equivalent circuit model of organic solar cells. Crystals 8 (5), 224.
Jain, A., Kapoor, A., 2004. Exact analytical solutions of the parameters of real solar cells using Lambert W-function. Sol. Energy Mater. Sol. Cells 81 (2), 269–277.
Jain, A., Kapoor, A., 2005. A new approach to study organic solar cell using Lambert W-function. Sol. Energy Mater. Sol. Cells 86 (2), 197–205.
Jiang, Q., Chu, Z., Wang, P., Yang, X., Liu, H., Wang, Y., Yin, Z., Wu, J., Zhang, X., You, J., 2017. Planar-structure Perovskite solar cells with efficiency beyond 21%. Adv. Mater. 29 (46), 1703852.
Jodlowski, A.D., Roldan-Carmona, C., Grancini, G., Salado, M., Ralaiarisoa, M., Ahmad, S., Koch, N., Camacho, L., de Miguel, D., Nazeeruddin, M.K., 2017. Large guanidinium cation mixed with methylammonium in lead iodide perovskites for 19% efficient solar cells. Nat. Energy 2 (12), 972–979.
Kumar, P., Gaur, A., 2013. Model for the J-V characteristics of degraded polymer solar cells. J. Appl. Phys. 113 (9), 094505.
Mazhari, B., 2006. An improved solar cell circuit model for organic solar cells. Sol. Energy Mater. Sol. Cells 90 (7), 1021–1033.
Meng, L., Zhang, Y., Wan, X., Li, C., Zhang, X., Wang, Y., Ke, X., Xiao, Z., Ding, L., Xia, R., Yip, H.L., Cao, Y., Chen, Y., 2018. Organic and solution-processed tandem solar cells with 17.3% efficiency. Science 361 (6407), 1094.
Ortiz-Conde, A., García-Sánchez, F.J., Muci, J., 2000. Exact analytical solutions of the forward non-ideal diode equation with series and shunt parasitic resistances. Solid-State Electron. 44 (10), 1861–1864.
Ortiz-Conde, A., Lugo-Muñoz, D., García Sánchez, F.J., 2012. An explicit multi-

exponential model as an alternative to traditional solar cell models with series and shunt resistances. IEEE J. Photovolt. 2 (3), 261–268.
Park, S., Heo, S.W., Lee, W., Inoue, D., Jiang, Z., Yu, K., Jinno, H., Hashizume, D., Sekino, M., Yokota, T., Fukuda, K., Tajima, K., Someya, T., 2018. Self-powered ultra-flexible electronics via nano-grating-patterned organic photovoltaics. Nature 561 (7724), 516.
Petti, L., Munzenrieder, N., Vogt, C., Faber, H., Buthe, L., Cantarella, G., Bottacchi, F., Anthopoulos, T.D., Troster, G., 2016. Metal oxide semiconductor thin-film transistors for flexible electronics. Appl. Phys. Rev. 3 (2), 021303.
Roland, P.J., Bhandari, K.P., Ellingson, R.J., 2016. Electronic circuit model for evaluating S-kink distorted current-voltage curves. Proc. IEEE 43rd Photovoltaic Specialists Conf. (PVSC).
Romero, B., del Pozo, G., Arredondo, B., 2012. Exact analytical solution of a two diode circuit model for organic solar cells showing S-shape using Lambert W-functions. Sol. Energy 86, 3026–3029.
Romero, B., del Pozo, G., Arredondo, B., Martín-Martín, D., Ruiz Gordoa, M.P., Pickering, A., Pérez-Rodríguez, A., Barrena, E., García-Sánchez, F.J., 2017. S-shaped I-V characteristics of organic solar cells: solving Mazhari's lumped-parameter equivalent circuit model. IEEE Trans. Electron Dev. 64 (11), 4622–4627.
Sahli, F., Werner, J., Kamino, B.A., Brauninger, M., Monnard, R., Paviet-Salomon, B., Barraud, L., Ding, L., Leon, J.J.D., Sacchetto, D., Cattaneo, G., Despeisse, M., Boccard, M., Nicolay, S., Jeangros, Q., Niesen, B., Ballif, C., 2018. Fully textured monolithic perovskite/silicon tandem solar cells with 25.2% power conversion efficiency. Nat. Mater. 17 (9), 820.
Sesa, E., Darwis, D., Zhou, X., Belcher, W.J., Dastoor, P.C., 2019. Experimental determination of the relationship between the elements of a back-to-back diode model for organic photovoltaic cells' S-shaped *I-V* characteristics and cell structure. AIP Adv. 9 (2), 025014.
Shockley, W., 1949. The theory of p-n junctions in semiconductors and p-n junction transistors. Bell Syst. Tech. J. 28 (3), 435–489.
Villalva, M.G., Gazoli, J.R., Filho, E.R., 2009. Comprehensive approach to modeling and simulation of Photovoltaic arrays. IEEE Trans. Power Electron. 24 (5–6), 1198–1208.
Wadsworth, A., Moser, M., Marks, A., Little, M.S., Gasparini, N., Brabec, C.J., Baran, D., McCulloch, I., 2019. Critical review of the molecular design progress in non-fullerene electron acceptors towards commercially viable organic solar cells. Chem. Soc. Rev. 48 (6), 1596–1625.
Wei, T., Yu, F., Huang, G., Xu, C., 2019. A particle-swarm-optimization-based parameter extraction routine for three-diode lumped parameter model of organic solar cells. IEEE Electron Device Lett. 40 (9), 1511–1514.
Xu, C., Yu, F., Lin, W., Huang, G., 2018. An improved organic solar cell lumped-parameter equivalent circuit model. Crystals 8 (7), 277.
Xu, F., Zhu, J., Cao, R., Ge, S., Wang, W., Xu, H., Xu, R., Wu, Y., Gao, M., Ma, Z., Jiang, Z., 2016. Elucidating the evolution of the current-voltage characteristics of planar organometal halide perovskite solar cells to an S-shape at low temperature. Sol. Energy Mater. Sol. Cells 157, 981–988.
Yoshikawa, K., Kawasaki, H., Yoshida, W., Irie, T., Konishi, K., Nakano, K., Uto, T., Adachi, D., Kanematsu, M., Uzu, H., Yamamoto, K., 2017. Silicon heterojunction solar cell with interdigitated back contacts for a photoconversion efficiency over 26%. Nat. Energy 2 (5), 17032.
Yu, F., Deng, W., Huang, J., Ma, X., Chen, S., 2016. An explicit physics-based I-V model for surrounding-gate polysilicon transistors. IEEE Trans. Electron Dev. 63 (3), 1059–1065.
Yu, F., Ma, X., Deng, W., Liou, J.J., Huang, J., 2017. A surface-potential-based drain current compact model for a-InGaZnO thin-film transistors in Non-Degenerate conduction regime. Solid-State Electron. 137 (11), 38–43.
Yu, F., Huang, G., Lin, W., Xu, C., 2019b. Lumped-parameter equivalent circuit model for S-shaped current-voltage characteristics of organic solar cells. IEEE Trans. Electron Devices 66 (1), 670–677.
Yu, F., Huang, G., Lin, W., Xu, C., Deng, W., Ma, X., Huang, J., 2019. Lumped-parameter equivalent circuit modeling of solar cells with S-shaped I-V characteristics. Solid-State Electron. 156 (6), 79–86.
Yu, F., Huang, G., Lin, W., Xu, C., Deng, W., Ma, X., Huang, J., 2019. Lumped-parameter equivalent circuit modeling of solar cells with S-shaped I-V characteristics. Solid-State Electron. 156 (6), 79–86.
Yu, F., Huang, G., Lin, W., Xu, C., 2019a. An analysis for S-shaped I-V characteristics of organic solar cells using lumped-parameter equivalent circuit model. Sol. Energy 177 (1), 229–240.
Zhou, Z., Xu, S., Song, J., Jin, Y., Yue, Q., Qian, Y., Liu, F., Zhang, F., Zhu, X., 2018. High-efficiency small-molecule ternary solar cells with a hierarchical morphology enabled by synergizing fullerene and non-fullerene acceptors. Nat. Energy 3 (11), 952–959.